Talanta 283 (2025) 127028

Contents lists available at ScienceDirect

Talanta

journal homepage: www.elsevier.com/locate/talanta

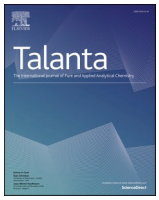

Nanozyme-based colorimetric and smartphone imaging advanced sensing platforms for tetracycline detection and removal in food

Xinli Guo [c,1], He Sun [c,1], Yuanzhen Yang [d], Wenbin Zhong [c], Mengmeng Wang [a], Guannan Wang [a,b], Yang Zhang [a,b,*]

[a] Shenyang Key Laboratory of Medical Molecular Theranostic Probes in School of Pharmacy, Shenyang Medical College, 146 Huanghe North Avenue, Shenyang, 110034, People's Republic of China
[b] Liaoning Province Key Laboratory for Phenomics of Human Ethnic Specificity and Critical Illness, Shenyang Medical College, Shenyang, 110034, People's Republic of China
[c] School of Basic Medicine, Shenyang Medical College, 146 Huanghe North Avenue, Shenyang, 110034, People's Republic of China
[d] School of Stomatology, Shenyang Medical College, 146 Huanghe North Avenue, Shenyang, 110034, People's Republic of China

ARTICLE INFO

Keywords:
Food analysis
Nanozymes
Tetracycline detection
Smartphone imaging
Colorimetric sensor

ABSTRACT

The presence of antibiotic residues poses a significant threat to food assurance, triggering widespread concerns. Therefore, the prompt and accurate detection and removal of antibiotic residues are essential for ensuring food safety. In this study, an aptmer modified triple-metal nanozyme (*apt*-TMNzyme) sensor was developed, which achieved a portable, visual, intelligent, and fast determination for tetracycline (TET). The proposed *apt*-TMNzyme exhibited willow leaf-like morphology, high specific surface area and excellent TET adsorption and removal properties. The experiments showed that the *apt*-TMNzyme had outstanding peroxidase activity and could catalyze the oxidation of 3,3′,5,5′-tetramethylbenzidine (TMB) to produce a blue product in the presence of H_2O_2, which provided a visual response signal to TET. This sensor was capable of quantifying TET within a concentration range of 0.2 nM–70 μM, achieving a detection limit of 7.1 nM under optimal conditions. When tested on real food samples, our sensor produced results that closely paralleled those achieved through high-performance liquid chromatography. To improve accessibility and user-friendliness, we also designed a colorimetric testing paper integrated with a smartphone application for intuitive and intelligent detection of TET, which enables the quantitative determination of TET in the concentration range of 0.003–60 μM, the detection limit was 5.1 μM. This integrated portable sensor not only streamlines the testing process, saving time and costs, but also offers a promising solution for rapid and sensitive detection of antibiotic residues.

1. Introduction

Tetracycline (TET), a type of effective broad-spectrum antibiotic, have been widely used in aquaculture industry, medicine, and animal husbandry because of its advantages of its oral administration, low cost, and high antimicrobial properties [1–4]. However, the stubborn TET molecule is difficult to be fully digested and metabolized in the body, leading to over 70 % of TET residues being released into the environment through urine and feces [5]. What makes it terrible is the excessive use of TET has led to a drastic increase in its residues in animal products and water bodies, which can be hazardous to human health and the environment, such as allergies, antibiotic resistance, teeth staining, gastrointestinal issues, and hepatotoxicity [6–8]. Several nations have instituted regulations concerning the maximum residue limit (MRL) of TET in food items. For example, the MRL of TET in milk is stipulated at 676 nmol/L by the US Food and Drug Administration and at 225 nmol/L by the European Union [9]. The maximum allowable residue of TET in China is 100 μg/kg, which corresponds to 225 nmol/L [10]. Therefore, it is crucial to develop a highly effective and responsive sensing platform for monitoring TET in order to safe guard the ecological environment and guarantee food safety, ultimately relieving people from antibiotic contamination. Until now, there are various analytical methods that

* Corresponding author. Shenyang Key Laboratory of Medical Molecular Theranostic Probes in School of Pharmacy, Shenyang Medical College, 146 Huanghe North Avenue, Shenyang, 110034, People's Republic of China.
E-mail address: zhangyangpro@symc.edu.cn (Y. Zhang).
[1] These authors contributed equally to this work.

https://doi.org/10.1016/j.talanta.2024.127028
Received 7 July 2024; Received in revised form 10 September 2024; Accepted 9 October 2024
Available online 19 October 2024

have been documented for TET analysis, including liquid chromatography-mass spectrometry (LC-MS) [11], high-performance liquid chromatography (HPLC) [12], and capillary electrophoresis (CE) [13]. However, numerous current analysis techniques suffer from drawbacks such as laborious sample preprocessing, dependence on specialized signal detection equipment, and prolonged response times. In contrast, colorimetric methods have attracted significant attention due to their simplified preparation, rapid and cost-efficient detection, independence from sophisticated instrumentation, and the convenience of direct visual inspection without the requirement for specialized tools. Hence, colorimetric sensor were considered a promising approach for detecting antibiotics due to their ease of use, affordability, heightened sensitivity, and selectivity. In addition, numerous technologies, such as membrane filtration, photocatalytic degradation, adsorption, and ion exchange, have been proposed for the removal of TET in water [14,15]. Adsorption technologies appear to be the most cost-effective and eco-friendly option [16]. The ongoing efforts to develop a strategy that integrate the detection and removal of TET emphasize the importance of devising a novel approach.

Nanozymes, a type of nanomaterial, exhibit the identical enzymatic properties and catalytic efficiency as natural enzymes, they are capable of catalyzing enzyme-substrate reactions under physiological conditions [17,18]. They are able to overcome the limitations of natural enzymes, such as high cost, production complexity [19], instability [20], and inherent environmental sensitivity which has restricted the use of naturally occurring enzymes [21]. In 2007, Yan et al. discovered that ferromagnetic nanoparticles (Fe_3O_4 NPs) exhibit peroxidase (POD)-like activity, demonstrating catalytic activity in comparison of protein/RNA, which acted as a POD in nature. They found that inorganic NPs can directly induce and speed up the oxidation of peroxidase substrates in the presence of hydrogen peroxide (H_2O_2) [22]. Furthermore, nanozymes can demonstrate equivalent kinetic properties to natural enzymes, facilitating the oxidation of substrates to generate colored products like *o*-phenylenediamine (OPD), 3,3′-diaminobenzidine (DAB), and 3,3,5,5-tetramethyl benzidine (TMB). The biological element within biosensors engages with target analytes, resulting in a signal that correlates with the concentration of the analytes. The transducer converts this signal into a measurement output that can be displayed on a readout or sent to a computer for analysis [23]. These encompass colorimetric, fluorometric, chemiluminescent, surface-enhanced Raman scattering, and electrochemical biosensors [24,25]. The improvement in signal amplification through nanozymes has driven progress in the effectiveness and sensitivity of many biosensor platforms. The oxidation of individual substrates results in distinct colors within aqueous solutions, which can be visually observed and distinguished based on their absorption spectra using a spectrophotometer [26]. The utilization of nanozymes for signal amplification has enhanced both the performance and sensitivity across a spectrum of biosensor platforms (encompassing colorimetric, fluorescent, chemiluminescent, surface-enhanced Raman scattering, and electrochemical biosensors) [27]. Due to their distinctive characteristics, nanozymes can additionally function as recognition receptors [28] or signal labels [29]. Building upon these novel characteristics, nanozymes are widely employed in environmental remediation efforts [30], antibacterial agents [31], biosensing [32], cytoprotection against cell biomolecules [33] and other applications.

Metal-organic frameworks (MOFs) have become increasingly popular in the field of biomedical applications. These nanomaterials are created through chemical reactions between metal ions or ion clusters and organic ligands, resulting in porous organic-inorganic hybrid materials. The specific surface area and porosity of MOFs play a crucial role in determining their catalytic performance. The high specific surface area and porosity of MOFs make them ideal for catalysis, adsorption, and gas storage, and they have been widely utilized in the detection of metal ions, dopamine, hydrogen peroxide (H_2O_2), and glucose in biological sensing applications. Metals in MOFs can mimic the catalytic properties of nanozymes, and their catalytic efficiency can be enhanced by using alloys made up of different elements [34–36]. Multiple metal nanozymes are more cost-effective and exhibit superior catalytic performance in biological processes compared to single-metal nanozyme [37].

Inspire of these, we employed *apt*-TMNzyme to develop a colorimetric probe for precise detection of TET residues in food. In addition, the high capacity removal of TET residues has also been completed, synchronously. However, detecting slight color changes with the naked eye is challenging and may not be accurate. To address this issue, smartphone applications are utilized for precise color recognition due to their advanced computing capabilities. The integration of colorimetric detection methods with smartphones has been successful in detecting TET residues in food, demonstrating the potential for smart inspection and field applications in various industries. This study builds upon existing research and provides a foundation for further advancements in food surveillance and public health safety.

2. Experimental section

2.1. Synthesis of TMNzyme

A standard solution was created by combining H_4DOT (24 mM), $Fe(NO_3)_3{\cdot}9H_2O$ (21 mM), $Co(NO_3)_2{\cdot}6H_2O$ (21 mM) and $Ni(NO_3)_2{\cdot}6H_2O$ (21 mM) with DMF (75 mL), ethanol (5 mL) and H_2O (5 mL). Subsequently, the blend was enclosed within a Teflon-coated stainless steel vessel and subjected to heating at 120 °C for 24 h. Following, the product was rinsed thrice with acetone and desiccated under vacuum conditions at 60 °C.

2.2. Synthesis of apt-TMNzyme

50 mg of TMNzyme was dispersed into 5.0 mL acetic acid-sodium acetate buffer solution (pH 4.0, 100 mM), followed by the addition of an equal amount of TET aptamer solution. The mixture was stirred for 4 h, then centrifuged at 12000 rpm for 10 min. The obtained TET aptamer modified TMNzyme (*apt*-TMNzyme) was then dried for reserve.

2.3. Analysis of POD-like activity

POD-like activity of *apt*-TMNzyme was investigated, 25 μL of 2.5 μg/mL *apt*-TMNzyme dispersion was added into acetate buffer (pH 4.0) containing 10 mM H_2O_2 and 0.5 mM TMB, the mixture was concussed at normal temperature for 35 min, followed by measuring the absorbance at 652 nm. The pH, temperature, and reaction time were also studied to assess their impact on the POD-like activity. Steady-state kinetic analysis was performed using acetate buffer (pH 4.0) with the addition of 25 μL of *apt*-TMNzyme (2.5 μg/mL). Various initial concentrations of TMB (ranging from 0.025 to 3 mM) or H_2O_2 (ranging from 0.01 to 20 mM) were examined under the ideal conditions (pH 4.0, temp 35 °C), and their absorbance at 652 nm was measured. A standard *Michaelis-Menten* curve was acquired, and the kinetic parameters were calculated employing the *Lineweaver-Burk* plot: $V = V_{max}\,[S]/(K_m + [S])$, where V and V_{max} represent the initial reaction rate and maximum reaction rate, respectively. $[C]$ is substrate concentration (TMB or H_2O_2), and K_m is *Michaelis* constant.

2.4. Catalytic mechanism

To explore how *apt*-TMNzyme exhibits POD-like activity, the catalytic mechanism was investigated by using isopropanol (IPA) scavengers to eliminate •OH and hydroethidine (HE) scavengers to eliminate $\bullet O^{2-}$. The absorbance value at 652 nm was measured in acetate buffer (pH 4.0) with 10 mM H_2O_2 and 0.5 mM TMB supplemented with different concentrations of IPA (0–4 mM). Additionally, acetate buffer (pH 4.0) with 1.0 mM H_2O_2 was supplemented with 0.5 mM HE, the fluorescence spectra at emission wavelengths of 590 nm were then measured.

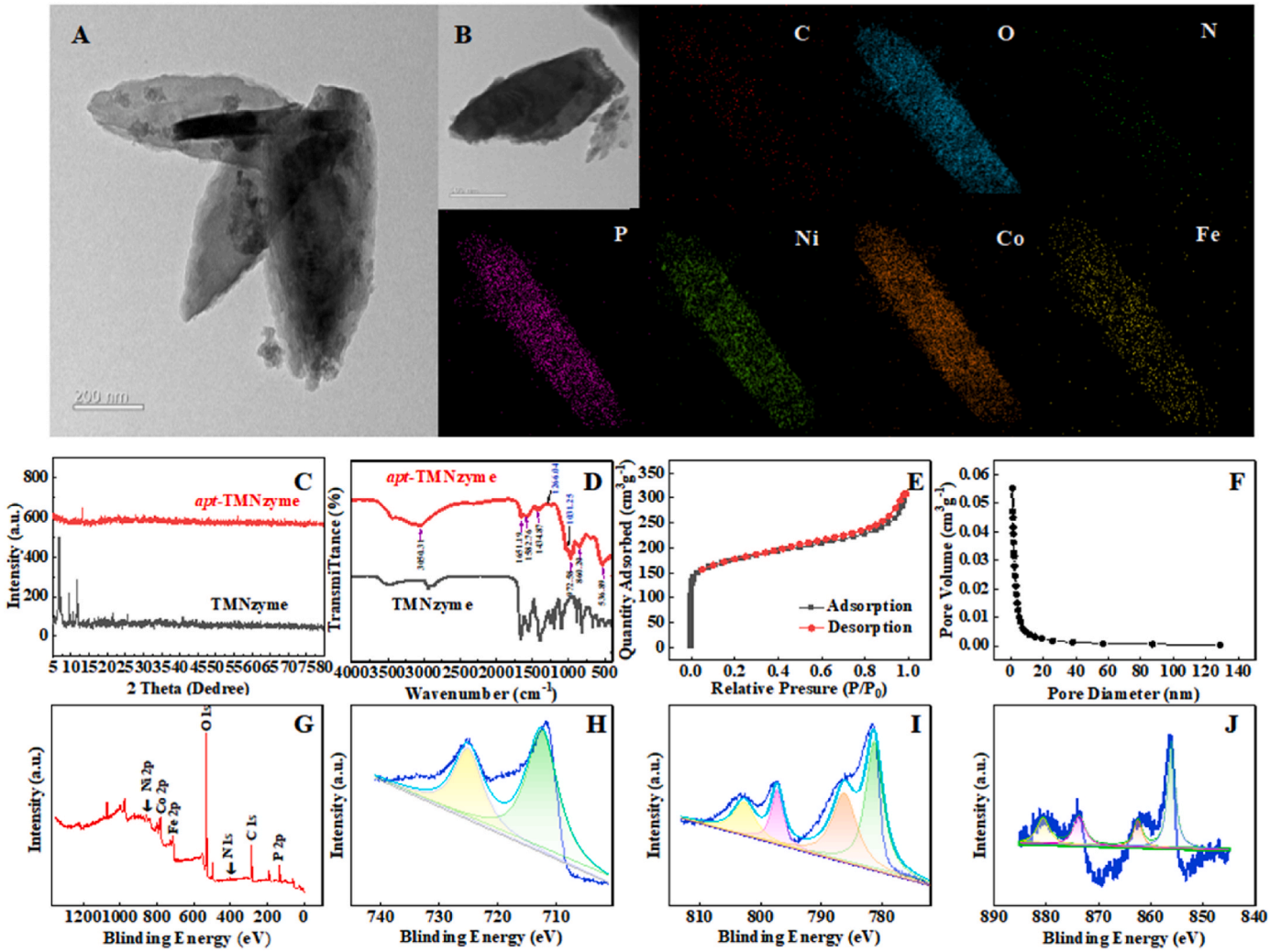

Fig. 1. (A) HR-TEM image of *apt*-TMNzyme and (B) corresponding elemental mappings showing the hierarchical elemental distributions of Ni, Co and Fe. (C) XRD patterns of TMNzyme and *apt*-TMNzyme. (D) FTIR measurements of TMNzyme and *apt*-TMNzyme. (E) N_2 adsorption/desorption isotherms and (F) the corresponding pore size distribution curve of the *apt*-TMNzyme. (G) XPS spectra of *apt*-TMNzyme and high-resolution spectra of Fe 2p (H), Co2p (I) and Ni 2p (J).

2.5. Colorimetric detection of TET

The TET solutions of varying concentrations (0.001 μM–100 μM) were added to a buffer solution (pH 4.0) containing *apt*-TMNzyme (2.5 μg/mL), TMB (0.5 mM), and H_2O_2 (10 mM). The total volume of the mixture was maintained at 200 μL, and the reaction was allowed to proceed for 35 min prior to assessing the absorbance at 652 nm. The solution obtained was also subjected to the same analysis as the control under identical conditions. For the selectivity and anti-interference experiments, two sets of experiments were conducted in parallel, with the interfering substances having the same concentration as TET besides general ions having four times and amino acids having two times the concentration of TET depended on above-mentioned reaction system.

2.6. TET adsorption by apt-TMNzyme

The adsorption properties of TET on *apt*-TMNzyme was examined. Adsorption kinetics were investigated by adding 50 μg/mL of *apt*-TMNzyme into 20 μg/mL of TET solution, and the concentration of residual TET in the supernatant was confirmed by UV–Vis spectroscopy. The adsorption capacity was studied by adding TET with different initial concentrations into *apt*-TMNzyme of 50 μg/mL solution. The following equation (1) was utilized to calculate the adsorption capacity.

$$Q_e = (C_0 - C_t)V / m \tag{1}$$

where Q_e (mg/g) represents the concentration of TET, C_0 (mg/L) represents the initial concentration of TET, while C_t (mg/L) represents the concentration of TET at time t. The volume of the reaction system is represented by V (L), while the amount of adsorbent is denoted by m (g).

Equations (2) and (3) describe the pseudo-first-order (PFO) and pseudo-second-order (PSO) models, respectively.

$$\ln(Q_e - Q_t) = \ln Q_e - k_1 t \tag{2}$$

$$\frac{t}{Q_t} = \frac{t}{Q_e} + \frac{1}{k_2 Q_e^2} \tag{3}$$

where Q_t (mg/g) stands for the adsorption capacity at any given time t (min), while Q_e (mg/g) represents the equilibrium adsorption capacity of the analyte. Additionally, k_1 (1/min) and k_2 (g/mg/min) denote the equilibrium rate constant of PFO and PSO adsorption, respectively.

Equations (4) and (5) present the fitting equations for the *Langmuir* model and *Freundlich* model, respectively.

$$\frac{C_e}{Q_e} = \frac{1}{Q_m k_L} + \frac{C_e}{Q_m} \tag{4}$$

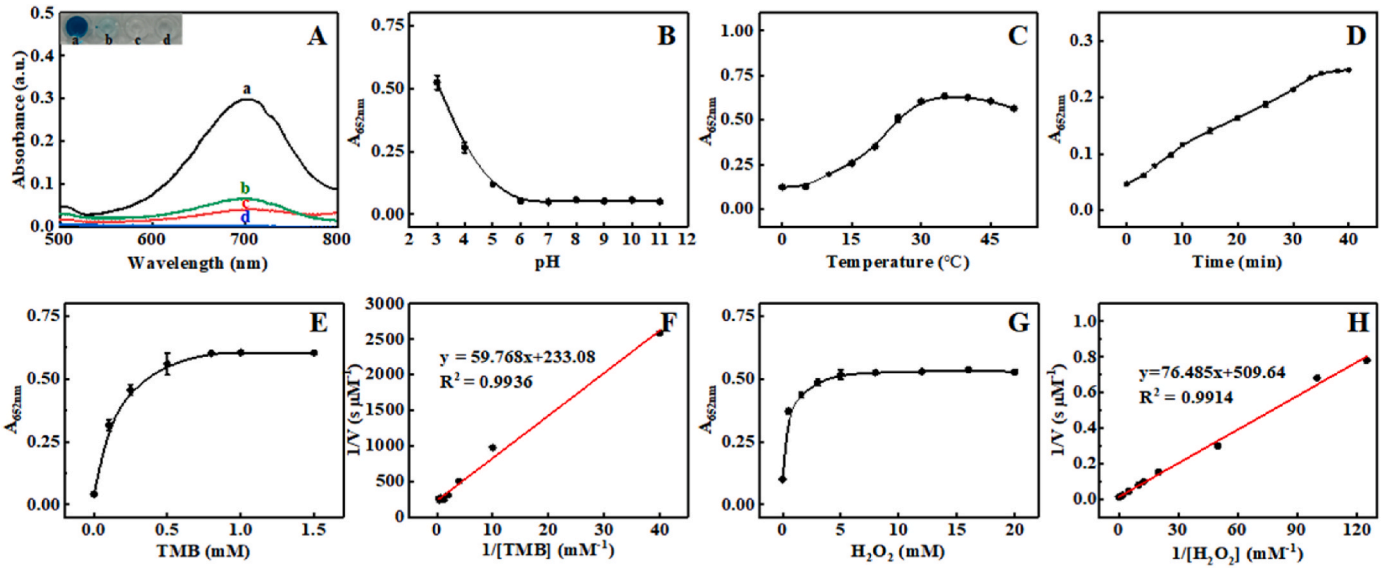

Fig. 2. (A) POD-like activity: typical absorption spectra of TMB, oxidation catalyzed by *apt*-TMNzyme and control groups in the presence of H_2O_2 at pH 4.0, and corresponding color changes (inset (a): *apt*-TMNzyme + H_2O_2 + TMB + Buffer, (b): H_2O_2 + TMB + Buffer, (c): *apt*-TMNzyme + H_2O_2 + Buffer, (d): *apt*-TMNzyme + TMB + Buffer). The effect of pH 3–11 (B), temperature (0 °C–50 °C) (C), reaction time (0–40 min) (D) on the POD-like activity. (E) The concentration of H_2O_2 was 10 mM and the TMB concentration varied and (F) Double reciprocal plots of the *Michaelis-Menten* equation from the activity date of the concentration of TMB. (G) The concentration of TMB was 0.5 mM and the H_2O_2 concentration varied and (H) Double reciprocal plots of the *Michaelis-Menten* equation from the activity date of the concentration of H_2O_2.

$$\ln Q_e = \ln k_F + \frac{1}{n}\ln C_e \quad (5)$$

where C_e (mg/L) and Q_e (mg/g) stand for the equilibrium concentration of TET and its adsorption capacity, respectively. Q_m (mg/g) represents the maximum theoretical adsorption capacity of TET per unit mass of samples. k_L (L/mg) and k_F are constants associated with *Langmuir* and *Freundlich* adsorption, respectively, while 1/n is an empirical parameter reflecting surface heterogeneity or adsorption intensity.

2.7. Preparation of colorimetric test strips

The procedure for preparing colorimetric test strips proceeded as follows: Whatman No. 1 chromatography paper was chosen as the foundational material and cut into 6 mm diameter circles using a hole puncher. These filter paper circles were then immersed in a solution containing *apt*-TMNzyme (2.5 μg/mL), H_2O_2 (10 mM) and TMB (0.5 mM) in a 5:4:2 vol ratio for 35 min before being air-dried. Subsequently, the test papers were dipped in a solution containing special concentration of TET for 15 min and air-dried again for TET detection. The *apt*-TMNzyme colorimetric paper exhibited noticeable color changes based on the concentration of TET and the test color was captured using a smartphone camera.

2.8. TET detection in authentic food samples

The determination of the LOD relied on the utilization of the 3σ method, and its calculation formula is: LOD = 3σ/k, where σ represents the standard deviation calculated from the blank samples (10 in total), and k is the gradient obtained when plotting the absorbance against the TET content.

2.9. TET detection in authentic food samples

To delve deeper into the sensor's practical application, we conducted tests on three varieties of honey (Robinia honey, Linden honey, and Loquat honey) obtained from a supermarket. The honey samples were diluted with H_2O (V/V, 1:20), and then filtrated using a 0.22 μm filter membrane. The filtered liquid was retained for future utilization. The honey samples containing different concentrations of TET were prepared by the method of standard addition (MSA), and the amount of TET in the authentic samples was determined. The recovery rate was calculated.

3. Results and discussion

3.1. Characterization

The process of synthesizing *apt*-TMNzyme initiated by combining a divalent metal (Ni^{2+}, Co^{2+}, Fe^{2+}) with H_4DOT in the solution comprising dimethylformamide, ethanol, and water. Subsequently, solvothermal crystallization of *apt*-TMNzyme is conducted at 120 °C for 24 h without the addition of any other substances. The initial exploration of the morphological and structural features of the synthesized *apt*-TMNzyme was conducted via TEM analysis. As depicted in Fig. 1A, the prepared *apt*-TMNzyme displayed willow leaf-like shape and uniform size. Furthermore, as displayed in the element mapping analysis in Fig. 1B, Ni, Co and Fe exhibit homogeneous distribution of across the carbon framework. According to the EDS analysis, the nanozyme contained Ni, Co, Fe, C, O, N, and P elements at atomic percentages of 4.81, 11.38, 2.43, 16.24, 54.16, 2.89, and 8.09, respectively.

The XRD pattern of the *apt*-TMNzyme exhibited two prominent and well-defined diffraction peaks at 2θ = 6.9° and 2θ = 11.8°, corresponding to the crystalline structure of the simulated TMNzyme (Fig. 1C). These peaks are believed to stem from various orientations in the lattice, causing an uneven state of organic ligands and metal ions within this crystal body, hence generating the characteristic diffraction patterns. Fig. 1D shows the FT-IR spectra of TMNzyme and *apt*-TMNzyme. The surface of the *apt*-TMNzyme was effectively modified with the phosphoric acid group of the aptamer, and asymmetric and symmetrical tensile vibrations appeared at 1266 cm^{-1} and 1031 cm^{-1}, respectively. Following aptamer modification, the peak observed at 537 cm^{-1} may be ascribed to vibrations between the metal and functional groups. Consequently, it can be inferred that the synthesis of *apt*-TMNzyme was successful prepared and the aptamer was effectively modified. N_2 adsorption/desorption isotherm of *apt*-TMNzyme showed

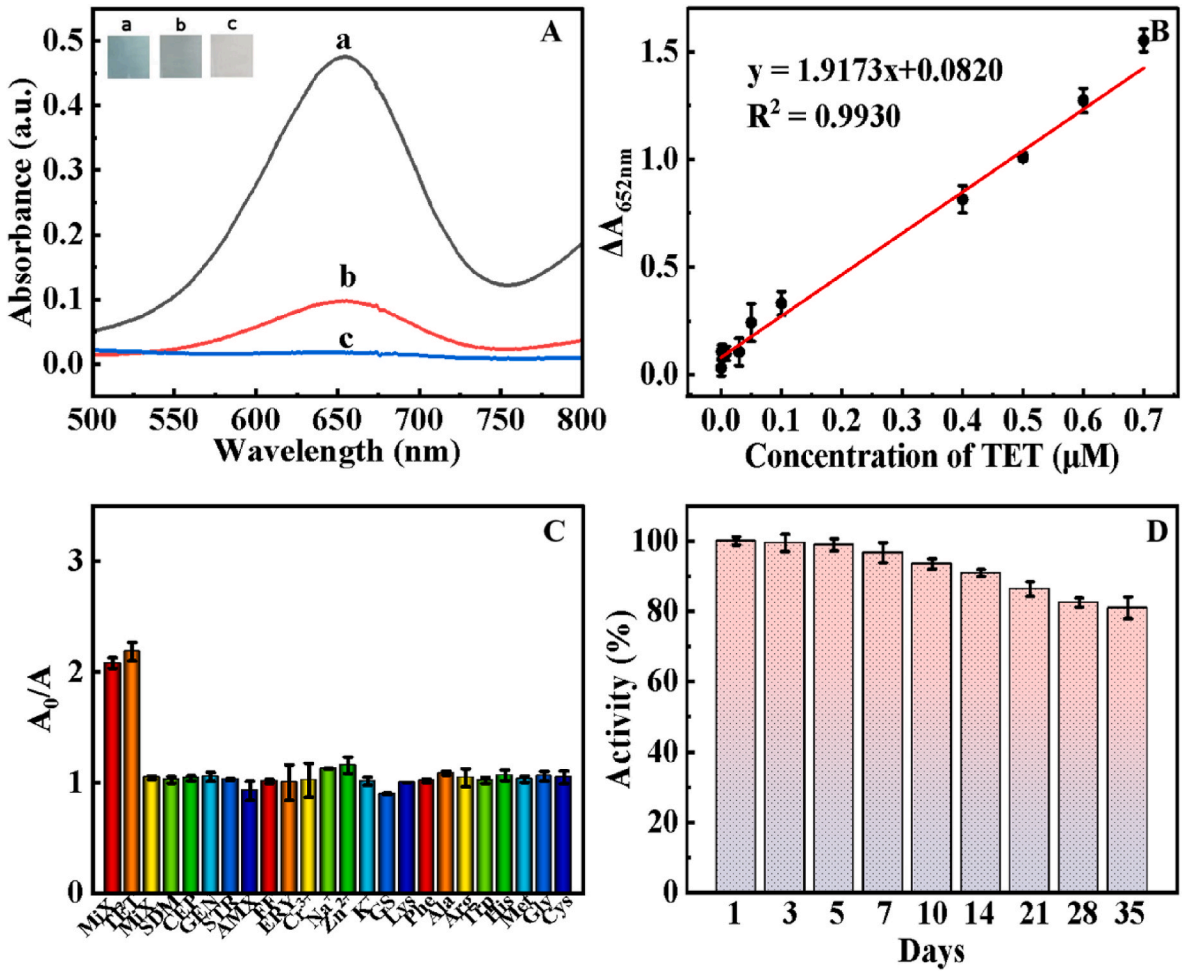

Fig. 3. (A) The absorbance of the catalytic reaction system with the addition of TET (inset (a): *apt*-TMNzyme + H_2O_2 + TMB + Buffer, (b): *apt*-TMNzyme + H_2O_2 + TMB + TET (0.1 mM) + Buffer (c): *apt*-TMNzyme + H_2O_2 + TMB + TET (0.3 mM) + Buffer). (B) The linear calibration plots for the quantitative determination of TET ($\Delta A = A_0$-A, where A_0 and A are the absorbance of the reaction system without and with TET. (C) Selectivity determination of *apt*-TMNzyme colorimetric sensor for TET. (D) The stability of POD-like activities for *apt*-TMNzyme five weeks.

the characteristics of mesopore with average pore size range from 3.4 nm to 4.3 nm (Fig. 1F). *Apt*-TMNzyme displayed a characteristic IV isotherm with an H_4 type hysteretic ring, and the specific surface area determined by the Brunauer-Emmett-Teller (BET) method was measured at 567.6 m^2/g, indicating that the porous structures of *apt*-TMNzyme persisted following the controlled modification of the aptamer (Fig. 1E). XPS analysis was carried out to assess the surface functional groups and elemental composition of *apt*-TMNzyme. As depicted in Fig. 1G, four non-metallic elements (C, O, N and P) and three metals elements (Fe, Co and Ni) all exhibit obvious signals in both wide and high-resolution XPS spectra. Two nuclear-level peaks, at 711.9 eV and 725.1 eV, appear in the Fe 2p spin orbit (Fig. 1H). The high-resolution Co 2p XPS spectra exhibit two binding energy peaks at 786.3 eV and 797.3 eV, representing the Co 2p 3/2 and Co 2p 1/3 ground states, respectively, alongside an oscillating satellite peak at 802.5 eV (Fig. 1I). In the Ni 2p XPS spectrum, peaks at 874.2 eV and 856.2 eV correspond to Ni 2p 3/2 and Ni 2p 1/2, respectively, accompanied by oscillatory satellite peaks observed at 862.2 eV and 880.9 eV (Fig. 1J). The XPS findings for *apt*-TMNzyme indicated the existence of bivalent metal ions, including Ni^{2+}, Co^{2+}, and Fe^{2+}.

3.2. Analysis of POD-like activity exhibited by apt-TMNzyme

The catalytic activities of TMNzyme and *apt*-TMNzyme were investigated for their POD-like activities using TMB as the substrate. A shift in color from colorless to blue was observed with the naked eye in the presence of H_2O_2 and nanozymes, with a maximum absorption peak at 652 nm. In contrast, control samples with only H_2O_2 or H_2O_2 & TMB without nanozymes showed minimal changes in color or absorbance (Fig. 2A). These demonstrated that TMNzyme and *apt*-TMNzyme could efficiently catalyze the oxidation of TMB with H_2O_2, exhibiting strong POD-like activity. Similarly, *apt*-TMNzyme also displayed enhanced POD-like activity, albeit to a lesser increase extent compared to TMNzyme (Fig. S1). Additionally, the activity was affected by pH, temperature, reaction time and the ideal conditions (pH 4.0, temp 35 °C, time 35 min) (Fig. 2B, C and 2D). The rate of catalytic reaction escalated with rising concentrations of TMB and H_2O_2 before entering a platform period, consistent with *Michaelis-Menten* kinetics (Fig. 2E and G). The *Michaelis-Menten* constants (K_m) for TMB and H_2O_2 substrates were 0.26 and 0.16 (Fig. 2F and H), respectively, highlighting the superior binding affinity and increased catalytic efficiency exhibited by the *apt*-TMNzyme with the substrates.

To explore the catalytic process, IPA or HE were utilized to validate the production of •OH or $•O^{2-}$ throughout the system reaction time. IPA could scavenge hydroxyl radicals. The absorbance value at 652 nm was observed in the IPA + H_2O_2 + TMB + *apt*-TMNzyme system. With the increase of the concentration of the active oxygen scavenger IPA (0, 1, 2, 3, 4 mM), the absorbance of the whole reaction system at 652 nm gradually decreased, indicating that •OH is the catalytic intermediate in the reaction system. (Fig. S2). The specific probe HE was employed to

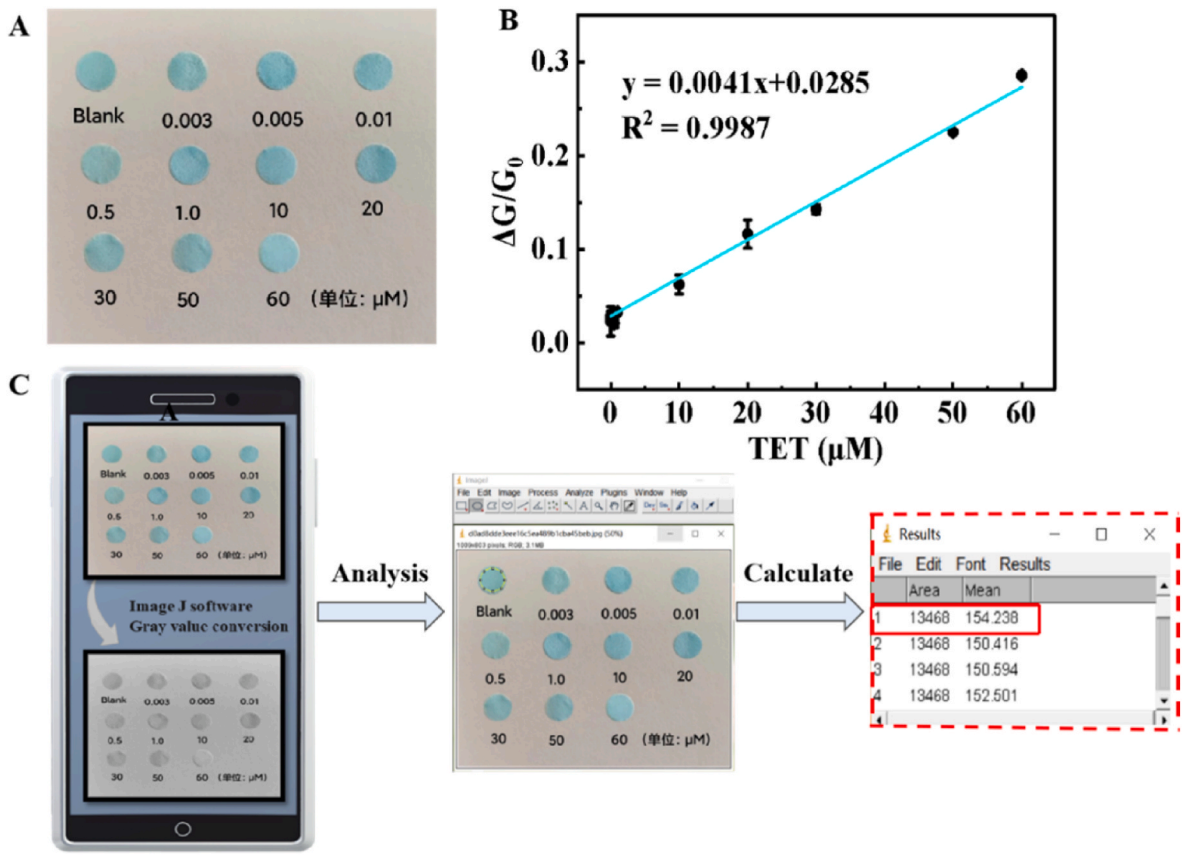

Fig. 4. (A) Colorimetric images of test papers after the reaction with different concentrations of TET (0, 0.003, 0.005, 0.01, 0.5, 1.0, 10, 20, 30, 50, 60 μM); (B) Linear relationship between $\Delta G/G_0$ values and TET concentrations (0.003–60 μM). (C) The schematic diagram of TET detection by the designed smartphone.

monitor $\bullet O^{2-}$ and generate ethidium, which emits strong fluorescence at around 590 nm. Nonetheless, no conspicuous fluorescent signal centered at 590 nm was detected for HE (Fig. S3), indicating there was no $\bullet O^{2-}$ produced during the catalytic oxidation process. In the case, the presence of triple metal Ni–Co–Fe sites at the catalyst interface facilitated substantial electron donation to the O atoms of H_2O_2, forming a bridging "Metal-*O*-O-Metal" complex that enables the continuous and stable activation of H_2O_2 by facilitating its barrierless dissociation to •OH. This activation mechanism lead to the generation of an electron-rich environment and multiple catalytic sites on the surface of *apt*-TMNzyme. These multiple sites enhance electron transfer and promote the spontaneous dissociation of H_2O_2 to •OH, resulting in a highly efficient Fenton-like catalytic reaction pathway and increased POD-like activity exhibited by *apt*-TMNzyme.

3.3. Detection of TET via colorimetry

The emission peak at 652 nm was selected as the signature signal for detection in this work. Fig. 3A demonstrates that the absorbance intensity at 652 nm decreased as the TET content increased under optimal conditions, which leads to the construction of a colorimetric sensor. Fig. 3B illustrates that the absorbance intensity exhibits a direct correlation with TET concentration within the ranges of 0.2 nM–70 μM, with a determined detection threshold of 7.1 nM. Compared with other alternative nanozyme materials, the amazing POD properties of *apt*-TMNzyme in this method contribute to the improvement of its sensitivity (Table S1). In Table S2, the *apt*-TMNzyme material prepared for detection of TET displays a broader detection range and a lower LOD compared to other analytical methods. Moreover, The sensor that was developed showed a color change from blue to colorless, making it easier to visually detect TET. To confirm the selectivity of the sensor for TET, various general metal ions and biological molecules were tested (Fig. 3C). It was found that only TET had a significant impact on the absorbance intensity and noticeable color changes, demonstrating that the *apt*-TMNzyme sensor has excellent selectivity for TET. Furthermore, the catalytic stability of *apt*-TMNzyme indicated that its catalytic activity remained above 80 % after five weeks (Fig. 3D), highlighting its considerable stability.

3.4. Smartphone-assisted sensitive detection of TET

Visualizing TET for detection could streamline the analysis procedure and is crucial for monitoring potentially hazardous factors. This study aimed to develop an economical TET test paper for convenient and visual testing purposes. The test strip changes color from blue to colorless as the amount of TET increased (Fig. 4A). Color recognition technology analyzes the RGB values of the image and the $\Delta G/G_0$ value showed a linear relationship with TET concentration in the range of 0.003–60 μM (Fig. 4B and C), with a detection limit of 5.1 μM under this condition. Smartphones were increasingly used for detection due to their portability and practicality. An application was designed to analyze color information captured by the smartphone for intelligent detection of TET. This method offers a new approach for designing portable devices and provides a solution for quantitative monitoring of TET for food safety.

3.5. Detection of real samples

Smartphone-assisted detection of TET in actual samples is of great significance for environmental protection and human health. The detection effect of *apt*-TMNzyme on TET in three varieties of honey (Robinia honey, Linden honey and Loquat honey) was analyzed. As

Table 1
Recovery test and precision of the determination of TET in real samples by colorimetric sensor.

Analyte	Honeys	Spiked (μM)	Picture	Smartphone (μM)	Recovery (%)	RSD (%, n = 3)
TET	Robinia honey	0.2		0.18	88.95	0.59
		2.0		1.94	96.92	0.88
		20.0		18.86	94.31	3.21
	Loquat honey	0.2	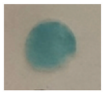	0.19	94.93	2.32
		2.0	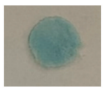	2.16	107.76	0.09
		20.0	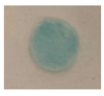	19.6	97.98	2.60
	Linden honey	0.20	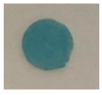	0.18	91.63	2.56
		2.0	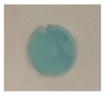	1.98	98.95	1.19
		20.0		21.12	105.61	3.71

shown in Table 1, the proposed smartphone-assisted sensor had good accuracy and could be used to monitor TET in real samples, with recoveries ranging from 88.95 % to 107.76 % and relative standard deviation (RSD) ranging from 0.09 % to 3.71 %. The findings exhibited strong correlation with those obtained through HPLC analysis and a newly devised colorimetric sensor in a buffered environment. Based on the information provided, it can be demonstrated that the *apt*-TMNzyme has the potential to function as a sensor for the precise and specific identification of TET in actual samples.

3.6. Adsorption experiments of TET

Further analysis was conducted to explore the adsorption characteristics of *apt*-TMNzyme onto TET. The effects of pH (Fig. S4) and contact time (Fig. S5) on TET adsorption were recorded, with optimal conditions were pH 9.0 and 30 min. The adsorption kinetics of TET onto *apt*-TMNzyme were examined, revealing an initial rapid increase in adsorption rate attributed to the plentiful adsorption sites on *apt*-TMNzyme, followed by a subsequent decline, reaching equilibrium within 30 min (Fig. 5A). For a more detailed examination of the adsorption kinetic curves, both the pseudo-first-order (Fig. 5B) and pseudo-second-order (Fig. 5C) kinetic models were utilized, with the latter demonstrating superior fitting for TET ($R^2 = 0.9988$). The research established that the adsorptive mechanism occurred via chemisorption, involving TET binding to the sites of *apt*-TMNzyme, with the respective dynamic parameters listed in Table S3. The impact of varying initial concentrations of TET on *apt*-TMNzyme was assessed using the adsorption isotherm (Fig. 5D). The adsorption mechanism was characterized using the *Langmuir* and *Freundlich* isotherm models (Fig. 5E and F). The results indicated that the *Langmuir* and *Freundlich* model accurately represents the TET data, and the relevant adsorption parameters were detailed in Table S4. This suggests that the interaction between *apt*-TMNzyme and TET binding sites involves chemical monolayer adsorption. As per the *Langmuir* adsorption model, the theoretical adsorption capacity of TET was calculated 94.339 mg/g, consistent with the actual capacity of 81.354 mg/g.

4. Conclusions

This work has successfully created a portable and sensitive colorimetric sensor that can detect TET quickly and accurately with the help of a smartphone. We first prepared willow leaf-like shape TMNzyme through an easy hydrothermal reaction and then used aptamer-functionalized TMNzyme as a colorimetric nanozyme-based probe to detect TET. By combining smartphones and test strips, we were able to reduce the cost, effort, and time needed for testing. Our colorimetric detection platform has a wide detection range (0.2 nM-70 μM), low LOD (7.1 nM), excellent selectivity and anti-interference performance under the optimal conditions. Smartphone imaging advanced sensing platforms was successfully applied for TET detection with satisfactory

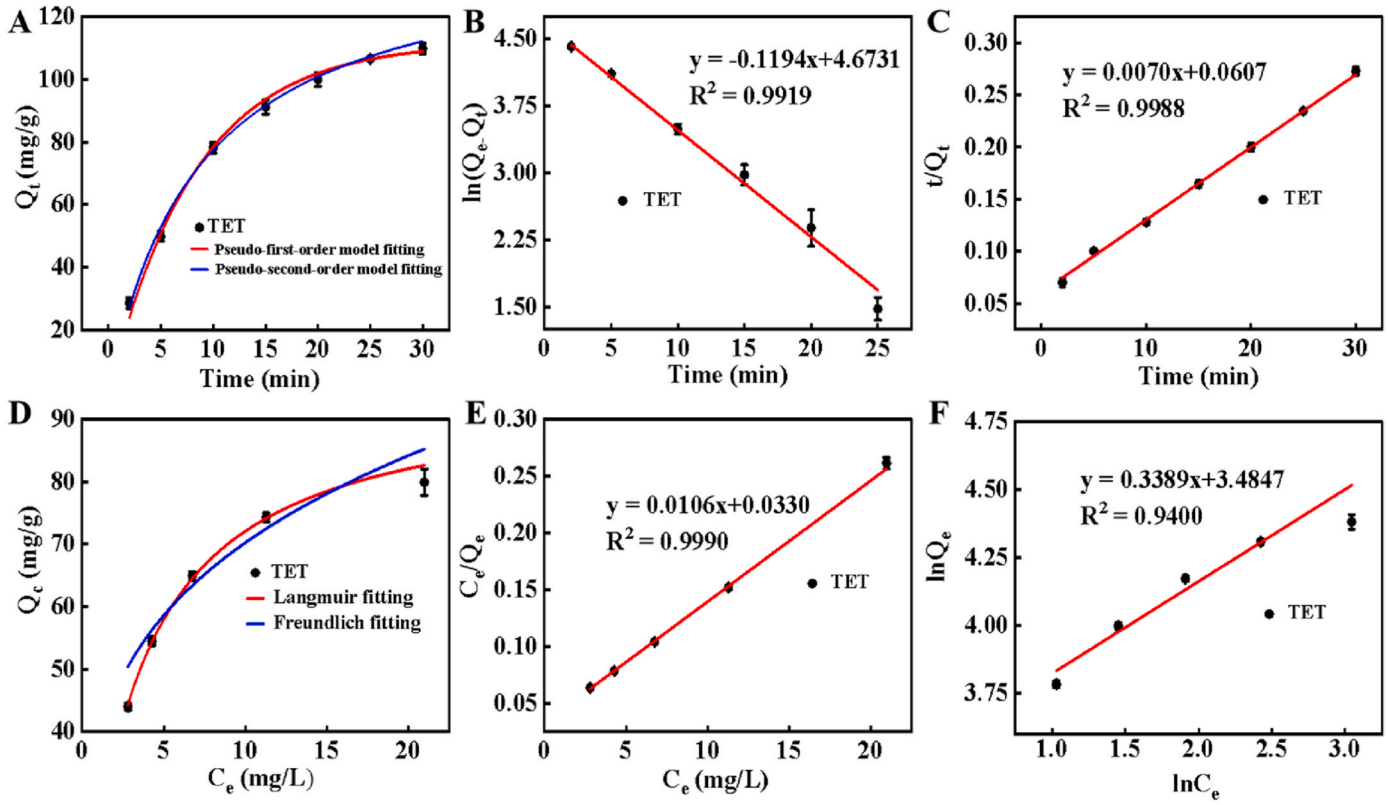

Fig. 5. (A) Adsorption of TET fitted by using pseudo-first-order and pseudo-second-order kinetic models. TET solution: 20 μg/mL; *apt*-TMNzyme: 50 μg/mL, pH 9.0, adsorption time: 30 min. The pseudo-first-order kinetic (B) and pseudo-second-order kinetic (C) isotherm fittings for TET on *apt*-TMNzyme. (D) The effect of TET initial concentration on *apt*-TMNzyme by the adsorption isotherm. The fitting curves of *Langmuir* model (E) for TET and *Freundlich* model (F) on *apt*-TMNzyme.

results. The successful testing of authentic samples confirmed the practicality of our portable detection platform, yielding satisfactory recoveries. Additionally, this sensor exhibits a high adsorption capacity for removing TET. This innovative approach lays the groundwork for the advancement and production of a novel nanozyme-based sensor, offering potential for efficient food contamination supervising via smartphones and the elimination of contaminants in real-world applications.

CRediT authorship contribution statement

Xinli Guo: Writing – original draft, Software, Methodology, Investigation, Data curation. **He Sun:** Validation, Software, Investigation, Data curation. **Yuanzhen Yang:** Investigation, Data curation. **Wenbin Zhong:** Investigation. **Mengmeng Wang:** Methodology, Investigation. **Guannan Wang:** Supervision, Conceptualization. **Yang Zhang:** Writing – original draft, Supervision, Methodology, Investigation, Funding acquisition, Conceptualization.

Declaration of competing interest

The authors declare the following financial interests/personal relationships which may be considered as potential competing interests:

Acknowledgments

The authors appreciate financial supports from the Shenyang Science and Technology Talent Special Project (RC230022), Natural Science Foundation of Liaoning Province (2023-MSLH-288), Science and Technology Project of Liaoning Provincial Department of Education (LJKR0556), Science Research Foundation of Education Department for Liaoning Province (LJKMZ20221790)

Appendix B. Supplementary data

Supplementary data to this article can be found online at https://doi.org/10.1016/j.talanta.2024.127028.

Data availability

Data will be made available on request.

References

[1] J. Guo, M. Huang, P. Gao, Y. Zhang, H. Chen, S. Zheng, T. Mu, X. Luo, Simultaneous robust removal of tetracycline and tetracycline resistance genes by a novel UiO/TPU/PSF forward osmosis membrane, Chem. Eng. J. 398 (2020) 125604.
[2] R.-Z. Wang, D.-L. Huang, Y.-G. Liu, C. Zhang, C. Lai, X. Wang, G.-M. Zeng, Q. Zhang, X.-M. Gong, P. Xu, Synergistic removal of copper and tetracycline from aqueous solution by steam-activated bamboo-derived biochar, J. Hazard Mater. 384 (2020) 121470.
[3] F. Yan, Z. Sun, J. Pang, Y. Jiang, W. Zheng, Functionalized carbon dots of thiazole derivatives based on inner filter effect for tetracyclines detection, Dyes Pigments 183 (2020) 108673.
[4] S. Zhang, Q. Sun, X. Liu, H. Li, J. Wang, M. Chen, Ratiometric fluorescence detection of tetracycline for tetracycline adjuvant screening in bacteria, Sensor. Actuator. B Chem. 372 (2022) 132687.
[5] J. Cao, Z. Yang, W. Xiong, Y. Zhou, Y. Peng, X. Li, C. Zhou, R. Xu, Y. Zhang, One-step synthesis of Co-doped UiO-66 nanoparticle with enhanced removal efficiency of tetracycline: simultaneous adsorption and photocatalysis, Chem. Eng. J. 353 (2018) 126–137.
[6] S. Cheng, P. Xie, Z. Yu, R. Gu, Y. Su, Enhanced adsorption performance of UiO-66 via modification with functional groups and integration into hydrogels, Environ. Res. 212 (2022) 113354.
[7] H. Yang, S. Hu, H. Zhao, X. Luo, Y. Liu, C. Deng, Y. Yu, T. Hu, S. Shan, Y. Zhi, H. Su, L. Jiang, High-performance Fe-doped ZIF-8 adsorbent for capturing tetracycline from aqueous solution, J. Hazard Mater. 416 (2021) 126046.
[8] S. Zeng, E. Kan, Sustainable use of $Ca(OH)_2$ modified biochar for phosphorus recovery and tetracycline removal from water, Sci. Total Environ. 839 (2022) 156159.

[9] W. Li, X. Zhang, X. Hu, Y. Shi, N. Liang, X. Huang, X. Wang, T. Shen, X. Zou, J. Shi, Simple design concept for dual-channel detection of ochratoxin A based on bifunctional metal-organic framework, ACS Appl. Mater. Interfaces 14 (2022) 5615–5623.
[10] B. Shi, X. Zhang, W. Li, N. Liang, X. Hu, J. Xiao, D. Wang, X. Zou, J. Shi, An intrinsic dual-emitting fluorescence sensing toward tetracycline with self-calibration model based on luminescent lanthanide-functionalized metal-organic frameworks, Food Chem. 400 (2023) 133995.
[11] Y. Chen, Electrochemical oxidation of low concentrated tetracycline (TC) in aqueous solution: operation optimization, degradation mechanisms, and detoxification efficiency, J. Environ. Chem. Eng. 12 (2024) 112604.
[12] Y.-H. Pang, Z.-Y. Lv, J.-C. Sun, C. Yang, X.-F. Shen, Collaborative compounding of metal-organic frameworks for dispersive solid-phase extraction HPLC-MS/MS determination of tetracyclines in honey, Food Chem. 355 (2021) 129411.
[13] G. Mu, H. Liu, L. Xu, L. Tian, F. Luan, Matrix solid-phase dispersion extraction and capillary electrophoresis determination of tetracycline residues in milk, Food Anal. Methods 5 (2012) 148–153.
[14] W. Bunmahotama, T. Lin, X. Yang, Prediction of adsorption capacity for pharmaceuticals, personal care products and endocrine disrupting chemicals onto various adsorbent materials, Chemosphere 238 (2020) 124658.
[15] Y. Yang, G. Zeng, D. Huang, C. Zhang, D. He, C. Zhou, W. Wang, W. Xiong, B. Song, H. Yi, S. Ye, X. Ren, In situ grown single-atom cobalt on polymeric carbon nitride with bidentate ligand for efficient photocatalytic degradation of refractory antibiotics, Small 16 (2020) 2001634.
[16] J. Ren, Z. Zhu, Y. Qiu, F. Yu, J. Ma, J. Zhao, Magnetic field assisted adsorption of pollutants from an aqueous solution: a review, J. Hazard Mater. 408 (2021) 124846.
[17] R.M. Tripathi, S.J. Chung, Phytosynthesis of palladium nanoclusters: an efficient nanozyme for ultrasensitive and selective detection of reactive oxygen species, Molecules 25 (2020) 3349.
[18] Y. Zhang, Y. Jin, H. Cui, X. Yan, K. Fan, Nanozyme-based catalytic theranostics, RSC Adv. 10 (2020) 10–20.
[19] R.M. Tripathi, D. Ahn, Y.M. Kim, S.J. Chung, Enzyme mimetic activity of ZnO-Pd nanosheets synthesized via a green route, Molecules 25 (2020) 2585.
[20] X. Zhang, G. Li, D. Wu, X. Li, N. Hu, J. Chen, G. Chen, Y. Wu, Recent progress in the design fabrication of metal-organic frameworks-based nanozymes and their applications to sensing and cancer therapy, Biosens. Bioelectron. 137 (2019) 178–198.
[21] Q. Liu, A. Zhang, R. Wang, Q. Zhang, D. Cui, A review on metal- and metal oxide-based nanozymes: properties, mechanisms, and applications, Nano-Micro Lett. 13 (2021) 154.
[22] L. Gao, J. Zhuang, L. Nie, J. Zhang, Y. Zhang, N. Gu, T. Wang, J. Feng, D. Yang, S. Perrett, X. Yan, Intrinsic peroxidase-like activity of ferromagnetic nanoparticles, Nature Nanotech 2 (2007) 577–583.
[23] S. Kubo, Y. Fuku, T. Shimamoto, A. Kuwayama, M. Ohya, H. Amano, T. Maruo, T. Goto, T. Komiya, K. Kadota, Vascular injury caused by retrieval of ruptured and detached balloon valvuloplasty catheter during transcatheter aortic valve replacement, JACC Cardiovasc. Interv. 10 (2017) 1593–1595.
[24] F. Arshad, N.F. Mohd-Naim, R. Chandrawati, D. Cozzolino, M.U. Ahmed, Nanozyme-based sensors for detection of food biomarkers: a review, RSC Adv. 12 (2022) 26160–26175.
[25] A. Mohamad, H. Teo, N.A. Keasberry, M.U. Ahmed, Recent developments in colorimetric immunoassays using nanozymes and plasmonic nanoparticles, Crit. Rev. Biotechnol. 39 (2019) 50–66.
[26] C.P. Kurup, M.U. Ahmed, Nanozymes towards personalized diagnostics: a recent progress in biosensing, Biosensors 13 (2023) 461.
[27] W. Wang, S. Gunasekaran, Nanozymes-based biosensors for food quality and safety, TrAC, Trends Anal. Chem. 126 (2020) 115841.
[28] Z. Su, T. Du, X. Liang, X. Wang, L. Zhao, J. Sun, J. Wang, W. Zhang, Nanozymes for foodborne microbial contaminants detection: mechanisms, recent advances, and challenges, Food Control 141 (2022) 109165.
[29] Y. Zhao, X. Wang, S. Pan, F. Hong, P. Lu, X. Hu, F. Jiang, L. Wu, Y. Chen, Bimetallic nanozyme-bioenzyme hybrid material-mediated ultrasensitive and automatic immunoassay for the detection of aflatoxin B_1 in food, Biosens. Bioelectron. 248 (2024) 115992.
[30] R. Singh, A. Umapathi, G. Patel, C. Patra, U. Malik, S.K. Bhargava, H.K. Daima, Nanozyme-based pollutant sensing and environmental treatment: trends, challenges, and perspectives, Sci. Total Environ. 854 (2023) 158771.
[31] R.M. Tripathi, B.R. Shrivastav, A. Shrivastav, Antibacterial and catalytic activity of biogenic gold nanoparticles synthesised by *Trichoderma harzianum*, IET Nanobiotechnol. 12 (2018) 509–513.
[32] R.M. Tripathi, S.J. Chung, Ultrasensitive and selective colorimetric detection of uric acid using peroxidase mimetic activity of biogenic palladium nanoparticles, Luminescence 38 (2023) 1330–1338.
[33] W. Li, Z. Liu, C. Liu, Y. Guan, J. Ren, X. Qu, Manganese dioxide nanozymes as responsive cytoprotective shells for individual living cell encapsulation, Angew. Chem. Int. Ed. 56 (2017) 13661–13665.
[34] Z. Chen, J.-J. Yin, Y.-T. Zhou, Y. Zhang, L. Song, M. Song, S. Hu, N. Gu, Dual enzyme-like activities of iron oxide nanoparticles and their implication for diminishing cytotoxicity, ACS Nano 6 (2012) 4001–4012.
[35] X. Liu, L. Yan, H. Ren, Y. Cai, C. Liu, L. Zeng, J. Guo, A. Liu, Facile synthesis of magnetic hierarchical flower-like Co_3O_4 spheres: mechanism, excellent tetra-enzyme mimics and their colorimetric biosensing applications, Biosens. Bioelectron. 165 (2020) 112342.
[36] M. Hu, K. Korschelt, P. Daniel, K. Landfester, W. Tremel, M.B. Bannwarth, Fibrous nanozyme dressings with catalase-like activity for H_2O_2 reduction to promote wound healing, ACS Appl. Mater. Interfaces 9 (2017) 38024–38031.
[37] K. Herget, P. Hubach, S. Pusch, P. Deglmann, H. Götz, T.E. Gorelik, I.A. Gural'skiy, F. Pfitzner, T. Link, S. Schenk, M. Panthöfer, V. Ksenofontov, U. Kolb, T. Opatz, R. André, W. Tremel, Haloperoxidase mimicry by CeO_{2-x} nanorods combats biofouling, Adv. Mater. 29 (2017) 1603823.